

## Near-field radiative heat transfer between doped-Si parallel plates separated by a spacing down to 200 nm

Jesse I. Watjen, Bo Zhao, and Zhuomin M. Zhang

Citation: [Applied Physics Letters](#) **109**, 203112 (2016); doi: 10.1063/1.4967384

View online: <http://dx.doi.org/10.1063/1.4967384>

View Table of Contents: <http://scitation.aip.org/content/aip/journal/apl/109/20?ver=pdfcov>

Published by the [AIP Publishing](#)

---

### Articles you may be interested in

[Electrically tunable near-field radiative heat transfer via ferroelectric materials](#)

Appl. Phys. Lett. **105**, 244102 (2014); 10.1063/1.4904456

[Graphene-assisted near-field radiative heat transfer between corrugated polar materials](#)

Appl. Phys. Lett. **104**, 251911 (2014); 10.1063/1.4885396

[Near-field radiative heat transfer between doped silicon nanowire arrays](#)

Appl. Phys. Lett. **102**, 053101 (2013); 10.1063/1.4790143

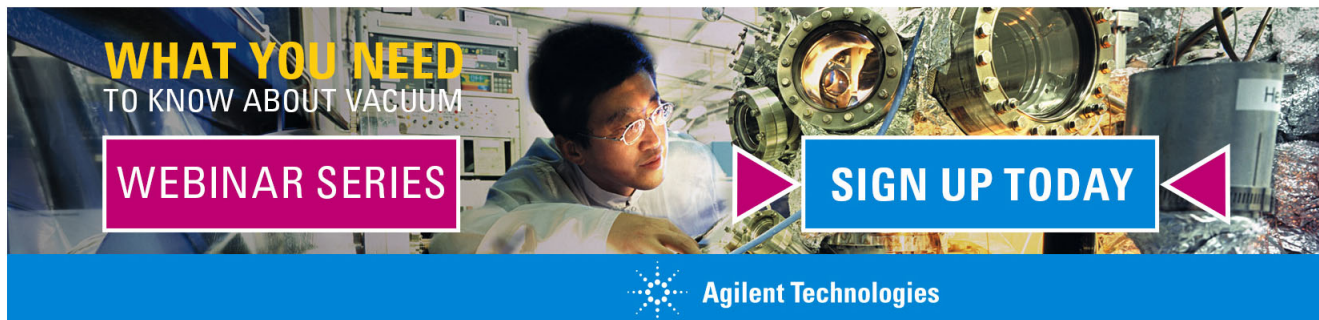
[Near-field radiative transfer based thermal rectification using doped silicon](#)

Appl. Phys. Lett. **98**, 113106 (2011); 10.1063/1.3567026

[Radiative heat transfer at nanoscale mediated by surface plasmons for highly doped silicon](#)

Appl. Phys. Lett. **95**, 231913 (2009); 10.1063/1.3271681

---

A promotional banner for Agilent Technologies. It features a background image of a person in a lab coat working with a piece of equipment. The text 'WHAT YOU NEED TO KNOW ABOUT VACUUM' is in yellow and white. Below it, a pink box says 'WEBINAR SERIES' and a blue box says 'SIGN UP TODAY'. The Agilent Technologies logo is at the bottom.

## Near-field radiative heat transfer between doped-Si parallel plates separated by a spacing down to 200 nm

Jesse I. Watjen,<sup>a)</sup> Bo Zhao,<sup>a)</sup> and Zhuomin M. Zhang<sup>b)</sup>

George W. Woodruff School of Mechanical Engineering, Georgia Institute of Technology, Atlanta, Georgia 30332, USA

(Received 4 July 2016; accepted 27 October 2016; published online 15 November 2016)

Heat transfer between two objects separated by a nanoscale vacuum gap holds great promise especially in energy harvesting applications such as near-field thermophotovoltaic systems. However, experimental validation of nanoscale radiative heat transfer has been largely limited to tip-plate configurations due to challenges of maintaining small gap spacing over a relatively large area. Here, we report measurements of heat transfer near room temperature between two 1 cm by 1 cm doped-Si parallel plates, separated by a vacuum gap from about 200 nm to 780 nm. The measured strong near-field radiative transfer is in quantitative agreement with the theoretical prediction based on fluctuational electrodynamics. The largest measured radiative heat flux is 11 times as high as the blackbody limit for the same hot and cold surface temperatures. Our experiments have produced the highest radiative heat transfer rate observed to date across submicron distances between objects near room temperature. *Published by AIP Publishing.*

[<http://dx.doi.org/10.1063/1.4967384>]

The increasing demand for sustainable energy leads to an urgent need for alternative energy harvesting methods with better performance than current technologies. Near-field radiative heat transfer is one of the most promising routes for boosting the efficiency and power output of energy harvesting systems such as thermophotovoltaics.<sup>1</sup> It has been shown that when two objects at different temperatures are brought within a distance much smaller than the characteristic wavelength of thermal radiation, the radiative heat flux can exceed the well-known blackbody limit governed by the Stefan-Boltzmann law by orders of magnitude.<sup>2–4</sup> This effect is caused by the coupling of forward and backward evanescent waves that opens the paths for photons to tunnel from the hot side to the cold side. Theoretically, near-field radiative heat flux scales up with  $d^{-2}$ , where  $d$  is the gap spacing between two parallel plates.<sup>2,5</sup> For energy harvesting applications, increasing the surface area and shrinking the gap spacing are both critical in order to achieve high radiative heating rates. While tremendous progress has been made in recent years toward experimental realization, measurements between planar surfaces with square-centimeter-sized areas at deep submicron gap distances are still quite challenging due to difficulties in controlling the gap spacing.<sup>6</sup> In this work, we experimentally measured the radiative heat transfer between two 1-cm<sup>2</sup> doped-Si plates separated by a vacuum gap spacing from  $(782 \pm 40)$  nm down to  $(200 \pm 80)$  nm. With careful control, thermal radiation dominates the heat transfer and the design may be extended to even larger heat transfer areas with other materials and thus may be implemented in applications such as near-field thermophotovoltaics,<sup>1,7</sup> thermal rectification,<sup>8,9</sup> thermal transistors,<sup>10</sup> and radiative refrigeration.<sup>11,12</sup>

Using complicated experiments enabled by scanning probe microscopy (SPM), researchers have measured the near-field radiative heat transfer between an SPM tip (or a small sphere) and a flat surface at gap distances down to tens of or even a few nanometers.<sup>3,4,13–17</sup> However, this type of configuration has a relatively small area where photon tunneling may occur and thus the heating rate is extremely limited, preventing it for use in applications that require a large photon flux. Continuous efforts have been made to overcome this limitation by measuring near-field thermal radiation between planar (or flat) surfaces, and significant progress has been made in recent years.<sup>18–26</sup> For example, Ito *et al.*<sup>24</sup> measured the near-field heat flux between two fused quartz substrates, with an area of 1.6 cm<sup>2</sup>, at gap spacings down to 500 nm. In the study by St-Gelais *et al.*,<sup>25</sup> a gap spacing near 40 nm was reached but the surface area was much smaller. Very recently, Song *et al.*<sup>26</sup> developed a microdevice that can achieve a spacing down to about 100 nm with surface areas about 50  $\mu\text{m}$  by 50  $\mu\text{m}$ . However, most of the reported experiments are still limited by either small heat transfer areas or relatively large gap spacings. These limitations can be understood if we consider that, for a perfectly flat 1-cm-wide piece to achieve 100 nm gap spacing, the angle of the piece cannot be off by more than  $6 \times 10^{-4}$  deg. Otherwise, contact between the two plates would occur at the end, and consequently, conduction would dominate the heat transfer. If the non-flatness of the sample surface is also considered, it is almost impossible to maintain a perfect nanometric gap over large areas. Therefore, there naturally exists a tradeoff between the surface area and the parallelism of the gap in practice. In order to benefit the real-world applications using near-field thermal radiation, it is imperative to explore a practical design that can reveal the near-field effect by keeping stringent parallelism between two planar surfaces with a relatively large heat transfer area and that can potentially be scaled up without too much complexity.

<sup>a)</sup>J. I. Watjen and B. Zhao contributed equally to this work.

<sup>b)</sup>Author to whom correspondence should be addressed. Electronic mail: zhuomin.zhang@me.gatech.edu

An experimental platform was developed in the present work for measuring the near-field heat transfer, as shown in Fig. 1(a). The spring presses the stack of layers onto a copper base to form a nearly one-dimensional heat flow path. The lateral dimensions of these layers, as well as the raised base plate, are 1 cm by 1 cm. On top of the stack lays a printed resistance heater (in red color online). A DC power supply provides 10–300 mW to the resistance heater. The heater is epoxied to a 1-mm-thick copper plate (in orange) that is gold plated to reduce the radiative heat loss. The sample (in blue) is sandwiched between two identical copper plates (using a thin layer of silver grease to ensure good thermal contact. A tiny hole drilled halfway through the side allows a thermocouple to be inserted on each copper plate to measure the hot-side and cold-side temperatures of the sample,  $T_1$  and  $T_2$ , respectively. The applied power generates a temperature difference ( $\Delta T_1 = T_1 - T_2$ ) about 2–30 K between the copper plates. A thermopile-type heat flux meter (HFM) is epoxied underneath the lower copper plate and atop the raised base plate. A calibrated silicon diode thermistor mounted on the base plate measures the absolute temperature of the heat sink ( $T_0$ ) with an uncertainty of 37 mK. The base plate is screw-fastened to the inside of a vacuum chamber. A thermocouple constructed using nickel-chromium (blue) and constantan (red) wires measures the temperature difference,  $\Delta T_2 = T_2 - T_0$ , in order to determine the cold plate temperature  $T_2$ , while the other measures the temperature difference between the copper plates  $\Delta T_1$  to obtain the absolute temperature  $T_1$ . Aluminum foil (not shown) surrounded the sample stage serves as a radiation shield to reduce the side heat loss. Together with the heat flux measured, the thermal conductance of the sample can be quantified and compared with theoretical predictions. A spring on top of the stack applies a quantifiable force on the sample.

The samples were constructed with two square pieces of doped-Si fabricated from double-side-polished wafers. The upper piece closer to the heater is called the radiation emitter while the lower piece is called the receiver throughout this paper. To create a desired gap spacing between the pieces, a two-dimensional array of  $\text{SiO}_2$  posts was fabricated on one piece using ultraviolet photolithography, as shown in Fig. 1(b).

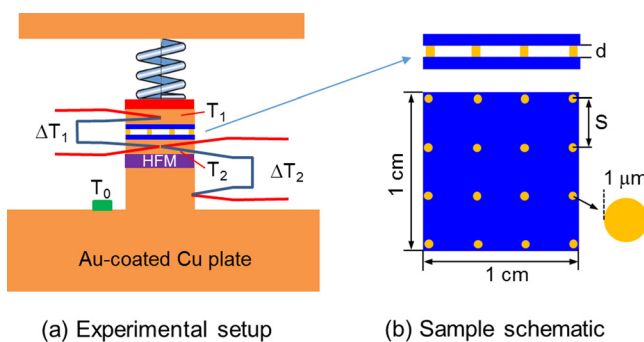


FIG. 1. Schematics of the experimental setup for measuring the near-field radiative heat transfer between flat plates and the structure of the sample. (a) The measurement stage that contains a stack of layers below the spring, namely, a heater, the upper Cu plate, the sample made of two doped-Si plates separated by a gap, the lower Cu plate, and a heat flux meter (HFM) mounted on a Cu heat sink. (b) The sample made of two doped-Si pieces separated by a sub-micron gap using  $\text{SiO}_2$  posts, where  $S$  is the distance between adjacent posts.

$\text{SiO}_2$  was chosen because of its low thermal conductivity, high mechanical strength, and ease of fabrication. The height of the posts varies between samples and ranges from 200 nm to 800 nm. An unpatterned piece was then mated together with the patterned piece in a cleanroom environment to form a sub-micron gap. The gap spacing is controlled by the height of posts and the applied force. Extremely flat wafers with a thickness approximately  $500 \mu\text{m}$  were employed, and a silicon dioxide layer was deposited on the back side of some wafers for bow reduction. The detailed fabrication process is described in the [supplementary material](#). Since the typical size of dust particles is on the order of micrometers, the small gap spacing naturally prevents particulate matter from entering the gap. While the posts maintain mechanical stability of the gap, they also introduce additional pathways for heat to conduct from the emitter to the receiver.

To measure the radiative heat transfer, it is preferred to ensure that thermal radiation is the dominant transfer mode across the sample. Note that the effect of gas conduction is eliminated by maintaining the pressure in the chamber below  $3 \times 10^{-4}$  Pa. Although near-field radiative transfer increases considerably as gap spacings approach the nanometer range, it is still orders of magnitude weaker compared to conduction heat transfer with the same cross-sectional area. Therefore, the number of the posts should be reduced as much as possible while maintaining the gap spacing mechanically. A photomask was made that contains four patterns with different spans between posts, i.e.,  $S$  equals to  $200 \mu\text{m}$ ,  $300 \mu\text{m}$ ,  $400 \mu\text{m}$ , and  $500 \mu\text{m}$ . With a post diameter of approximately  $1 \mu\text{m}$ , it is estimated that more than half of the conductance is due to radiation when  $S$  exceeds about  $300 \mu\text{m}$  (see [supplementary material](#) for details).

Even though the thermal grease was applied, contact resistance could not be completely removed. Thus, after measuring the samples under vacuum, the chamber was returned to ambient pressure where gas conduction across the gap dominates and the thermal resistance of the sample is negligible due to the large thermal conductivity of silicon. Thermal resistances of the Cu plates are also negligible. Thus, the contact resistance at the copper-silicon interfaces can be obtained based on the measured  $T_1$  and  $T_2$  when the chamber is at ambient pressure. It is assumed that the contact resistance is the same above and below the sample. The contact resistance value, ranging from 4 to 9 K/W across each Si-Cu interface, was used to deduce the temperatures of the two Si pieces, i.e., the emitter ( $T_H$ ) and receiver ( $T_L$ ). The radiative heat transfer rate,  $q_{\text{rad}}$ , is obtained by excluding the conduction from the total heat transfer rate measured by the heat flux meter with the assumption that all posts have the same height as the gap spacing. The radiative heat transfer coefficient is calculated from

$$h_{\text{rad}} = \frac{q_{\text{rad}}/A}{\Delta T}, \quad (1)$$

where the area  $A = 1 \text{ cm}^2$ , by neglecting the posts, and  $\Delta T = T_H - T_L$ .

Figure 2 displays  $q_{\text{rad}}$  for three different gap spacings versus  $\Delta T$ . The isolated solid symbols represent the measured results with uncertainty bounds indicated by the error bars.

The dashed lines are from the calculation with the shaded region indicating the uncertainty bounds. Fluctuational electro-dynamics was used to calculate the near-field radiative heat transfer as discussed in the [supplementary material](#). The large enhancement in nanoscale thermal radiation is attributed to the excitation of coupled surface plasmon polaritons.<sup>1,2</sup> The uncertainty of the theoretical calculation is mainly due to the determination of the gap spacing. It can be seen that good agreement exists between the measurement and calculation: the differences are 5%, 17%, and 37% for gap spacing ( $d$ ) of 762 nm, 350 nm, and 200 nm, respectively. These are all within the combined uncertainties of the experiment and calculation. As  $d$  gets smaller, not only does  $q_{\text{rad}}$  become larger but also  $h_{\text{rad}}$  increases as evidenced by the increased slope. For a given gap spacing, the curve is not linear since measured  $h_{\text{rad}}$  increases slightly as the temperature increases. Different  $\Delta T$  is created by controlling the power of DC power supply. However, due to radiation from the top of the heater and conduction through the spring, not all the heating power flows down across the sample. For example, with a 265 mW power provided by the DC power supply, about 191 mW (134 mW due to radiation and 57 mW due to conduction) pass through the 200 nm sample, creating a  $\Delta T = 16.5^\circ\text{C}$ . The value  $q_{\text{rad}} = 134$  mW is considered the highest radiation heat transfer rate through submicron gap spacings measured to date.

Figure 3 illustrates the experimental results for  $h_{\text{rad}}$  for 14 measurements at different gap spacings. The measured data are presented as filled symbols with error bars, while the calculated values at the same temperature and gap spacings are shown as open circles. The 14 measurements were conducted using seven different samples. Some of the samples were measured under different applied forces since the gap spacing is sensitive to the applied force. Each shape of the solid symbols represents a different sample under

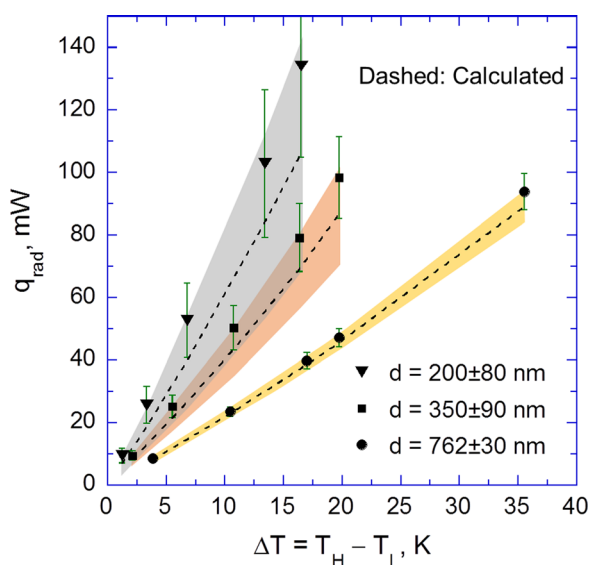


FIG. 2. Radiative heat transfer rate ( $q_{\text{rad}}$ ) for three different gap spacings as a function of the temperature difference. The filled symbols are the measured results with error bars. The dashed line represents the calculated  $q_{\text{rad}}$  based on the measured temperatures and gap spacing using fluctuational electro-dynamics. The shaded regions show the uncertainty bounds of the calculated  $q_{\text{rad}}$ .

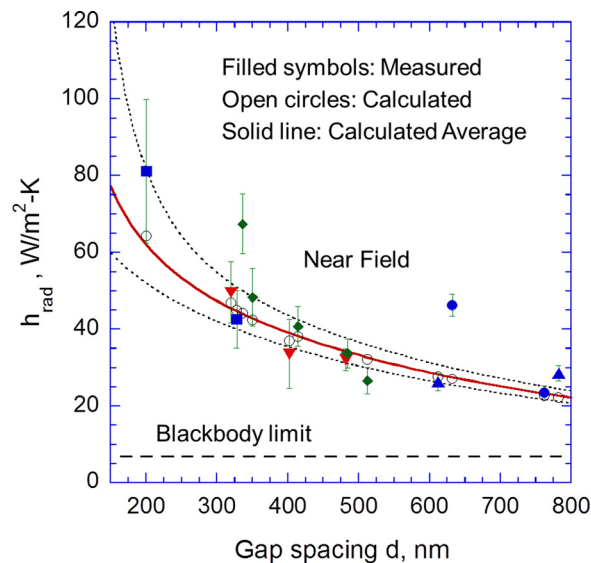


FIG. 3. Radiative heat transfer coefficient ( $h_{\text{rad}}$ ) for 14 measurements at different gap spacings with  $\Delta T$  ranging from 15.2 K to 19.2 K (except for the one at 402 nm spacing for which  $\Delta T = 9.8$  K). The filled symbols represent the measured results with error bars. Each shape denotes a specified sample under certain applied forces. The open circle is the calculated  $h_{\text{rad}}$  for each sample at the measured  $T_{\text{H}}$  and  $T_{\text{L}}$ . The solid red line is the  $h_{\text{rad,avg}}$  calculated from the average  $T_{\text{H}}$  (318.5 K) and  $T_{\text{L}}$  (302.3 K). The dotted lines are the uncertainty bounds of  $h_{\text{rad,avg}}$ . The dashed horizontal line is for two blackbodies at the average  $T_{\text{H}}$  and  $T_{\text{L}}$ .

specified applied forces. For example, the sample represented by the green diamond symbols is measured under different forces ranging from 0 mN to 200 mN to control the gap spacing from about 512 nm to 336 nm. The applied force and the sample used for each measurement are given in Table S1 (see [supplementary material](#)). The solid (red) line represents the calculated results using the average  $T_{\text{H}}$  and  $T_{\text{L}}$  (i.e., 318.5 K and 302.3 K, respectively) of all measurements and plotted as a function of gap spacing. The two dotted lines represent the calculation uncertainty bounds. The horizontal dashed line is the blackbody limit using the average  $T_{\text{H}}$  and  $T_{\text{L}}$ . A reasonable agreement between the experiment and calculation can be seen from Fig. 3. Note that  $h_{\text{rad}}$  increases as  $d$  decreases, reaching a value of  $81.2$   $\text{W}/\text{m}^2\text{-K}$  that is about 11 times that of the blackbody limit at the same emitter and receiver temperatures. This value is nearly twice as high as those reported by Ito *et al.*<sup>24</sup> between fused quartz at their smallest gap spacing of 500 nm. The measured results at distances of 336 nm and 632 nm are much higher than the predictions; possible reasons for the disagreement will be discussed later.

While the  $\text{SiO}_2$  posts maintain the gap between the two Si pieces, the gap spacing is not necessarily equal to the height of the posts. In the experiment, the gap spacing can be higher than the post height by tens to a few hundreds of nanometers. Since the height of the posts are nearly uniform across the sample and their top surfaces are flat within about 30 nm based on measurements, possible reasons for the discrepancy are the residual bow or warp, unevenness of the post heights due to etching, and particles on the order of tens of nanometers. This effect also makes the gap spacing sensitive to external forces applied on the sample similarly as with a spring, offering a possible way to further control the

gap spacing through nearly elastic deformation. Therefore, in the experiment, we used a Fourier-transform infrared spectrometer (FTIR) to measure the reflectance of each sample to quantify the gap spacing prior to the heat transfer measurement. In some more recent measurements, different forces were applied for both the FTIR measurement and the heat transfer measurement, allowing the gap spacing to be adjusted.

As mentioned before, the sample contains two doped-Si slabs, about  $500\ \mu\text{m}$  thickness, sandwiching a thin layer of vacuum or air. The spectral reflectance depends on the thickness of the middle layer due to interference effects, and thus the reflectance spectrum can be used to determine the gap spacing. The reflectance is insensitive to the thickness of the Si slabs since the FTIR resolution is not high enough to distinguish the interference fringes in the Si slab, which can be treated as incoherent.<sup>5</sup> This technique, however, requires the Si slab to be transparent at least in a certain frequency range for the infrared radiation to penetrate through and generate a distinguishable interference pattern. Meanwhile, the material is required to be opaque in the mid- and far-infrared range to have a considerable radiative heat flux. Calculations suggest that, for  $500\text{-}\mu\text{m}$ -thick Si wafers, a doping concentration from  $1 \times 10^{18}$  to  $3 \times 10^{18}\ \text{cm}^{-3}$  can still be transparent at wavenumbers from  $2000\ \text{cm}^{-1}$  to  $10000\ \text{cm}^{-1}$  for FTIR measurements of the gap spacing, while at the same time can have sufficient free-carrier absorption at longer wavelengths for near-field radiative transfer enhancement.<sup>27,28</sup> Si wafers doped with antimony atoms of  $2 \times 10^{18}\ \text{cm}^{-3}$  concentration were purchased from a commercial vendor. Their optical constants are extracted from the measured reflectance and transmittance of the wafer as well as extended to the mid- and far-infrared using a Drude model (see [supplementary material](#)). The doped-Si pieces can be treated as semi-infinite when considering the near-field radiative heat transfer, so that the backside oxide films and other materials at the contact have negligible effects on the radiative heat transfer. However, the oxide film does affect the measured FTIR spectrum as discussed next.

A fixture was manufactured and mounted on the reflectance accessory of the FTIR in order to apply different forces on the sample during the reflectance measurement in a similar manner as shown in Fig. 1(a) for heat transfer measurements. Considering the yield stresses of the  $\text{SiO}_2$  and Si, the applied force on the sample is limited to 200 mN. The gap distance is determined using a least-squares method by comparing the measured reflectance spectrum with the theoretical curves at different gap spacings. Figure 4 shows the measured and calculated reflectance spectra for three different gap spacings. The spectrum for the sample with 200 nm spacing is different since the patterned and the unpatterned piece have a silicon dioxide film of 595 nm and 785 nm, respectively, on the back sides. The gap spacing is determined such that the predicted spectrum at this gap spacing yields the smallest standard error of estimate compared to the measurement as discussed in the [supplementary material](#). After the gap spacing is fully characterized, the sample is mounted in the experimental setup to measure the thermal conductance with a force applied to achieve a desired gap spacing. While good agreement between the measurement and calculation is obtained for most data points shown in Fig. 3, it

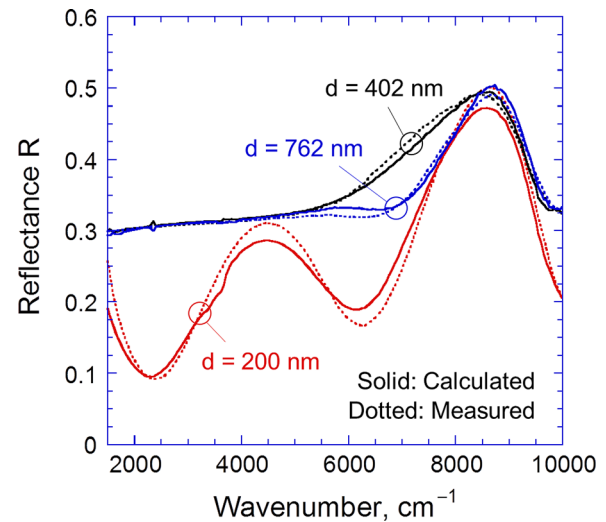


FIG. 4. Reflectance spectra for three samples with different gap spacings. The sample with a spacing of 200 nm has an oxide film of 595 nm and 785 nm on the back sides of the patterned and the unpatterned pieces, respectively.

should be noted that for the sample shown with diamond symbols, the reflectance spectra for  $260\ \text{nm} < d < 340\ \text{nm}$  are almost indistinguishable, which may explain the deviation of the measured result at 336 nm spacing. A smaller gap spacing than the prescribed value would increase the calculated  $h_{\text{rad}}$  and decrease the measured  $h_{\text{rad}}$ , making the agreement between them possible. This can be a limitation of using doped-Si in the current experiment, but may be alleviated when other materials are used. Note that the force needs to be applied with great care since an uneven distribution of forces can cause the sample to deform nonuniformly and create local bow that makes the gap spacing smaller than that determined by FTIR. This can cause a larger measured  $h_{\text{rad}}$  than the calculated value and could be the reason for the deviation of measurement at 632 nm spacing. Because the sample is contaminated by the grease after the thermal conductance measurement, they cannot be remeasured on the FTIR. The result for the 632 nm spacing is shown to stress the importance of handling the sample in the experiments.

The experimental results presented here demonstrate that the near-field effect can be probed with a heat transfer area at the square-centimeter scale and gap spacings down to about 200 nm. The high heat transfer rate achieved from this study may facilitate practical applications in energy conversion and thermal management devices based on near-field thermal radiation. With the development of this technique and future improvements, it is expected that accurate measurements can be made possible between various materials and nanostructures with even larger heat transfer areas that can potentially yield even stronger near-field heat transfer. Experiments of this nature and insights from such studies may signify breakthroughs in applications of near-field thermophotovoltaics, radiative cooling and refrigeration, and thermal rectifiers or transistors.

See [supplementary material](#) for details of sample fabrication, dielectric function, gap spacing determination, uncertainty analysis, and theoretical calculations.

This work was primarily supported by the U.S. Department of Energy, Office of Science, Basic Energy Science (DE-FG02-06ER46343). B.Z. and Z.M.Z. were also supported by the National Science Foundation (CBET-1235975; CBET-1603761). The facilities at Georgia Tech's Institute for Electronics and Nanotechnology (IEN) were used for the sample fabrication and some characterizations.

- <sup>1</sup>S. Basu, Y.-B. Chen, and Z. M. Zhang, *Int. J. Energy Res.* **31**, 689 (2007).
- <sup>2</sup>C. J. Fu and Z. M. Zhang, *Int. J. Heat Mass Transfer* **49**, 1703 (2006).
- <sup>3</sup>S. Shen, A. Narayanaswamy, and G. Chen, *Nano Lett.* **9**, 2909 (2009).
- <sup>4</sup>E. Rousseau, A. Siria, G. Jourdan, S. Volz, F. Comin, J. Chevrier, and J.-J. Greffet, *Nat. Photonics* **3**, 514 (2009).
- <sup>5</sup>Z. M. Zhang, *NanolMicroscale Heat Transfer* (McGraw-Hill, New York, 2007).
- <sup>6</sup>X. L. Liu, L. P. Wang, and Z. M. Zhang, *Nanoscale Microscale Thermophys. Eng.* **19**, 98 (2015).
- <sup>7</sup>R. S. DiMatteo, P. Greiff, S. L. Finberg, K. A. Young-Waithe, H. K. H. Choy, M. M. Masaki, and C. G. Fonstad, *Appl. Phys. Lett.* **79**, 1894 (2001).
- <sup>8</sup>C. R. Otey, W. T. Lau, and S. Fan, *Phys. Rev. Lett.* **104**, 154301 (2010).
- <sup>9</sup>L. P. Wang and Z. M. Zhang, *Nanoscale Microscale Thermophys. Eng.* **17**, 337 (2013).
- <sup>10</sup>P. Ben-Abdallah and S.-A. Biehs, *Phys. Rev. Lett.* **112**, 044301 (2014).
- <sup>11</sup>K. Chen, P. Santhanam, S. Sandhu, L. Zhu, and S. Fan, *Phys. Rev. B* **91**, 134301 (2015).
- <sup>12</sup>X. L. Liu and Z. M. Zhang, *Nano Energy* **26**, 353 (2016).
- <sup>13</sup>A. Kittel, W. Müller-Hirsch, J. Parisi, S.-A. Biehs, D. Reddig, and M. Holthaus, *Phys. Rev. Lett.* **95**, 224301 (2005).
- <sup>14</sup>S. Shen, A. Mavrokefalos, P. Sambegoro, and G. Chen, *Appl. Phys. Lett.* **100**, 233114 (2012).
- <sup>15</sup>J. Shi, P. Li, B. Liu, and S. Shen, *Appl. Phys. Lett.* **102**, 183114 (2013).
- <sup>16</sup>K. Kim, B. Song, V. Fernández-Hurtado, W. Lee, W. Jeong, L. Cui, D. Thompson, J. Feist, M. T. H. Reid, F. J. García-Vidal, J. C. Cuevas, E. Meyhofer, and P. Reddy, *Nature* **528**, 387 (2015).
- <sup>17</sup>B. Song, Y. Ganjeh, S. Sadat, D. Thompson, A. Fiorino, V. Fernández-Hurtado, J. Feist, F. J. Garcia-Vidal, J. C. Cuevas, P. Reddy, and E. Meyhofer, *Nat. Nanotechnol.* **10**, 253 (2015).
- <sup>18</sup>L. Hu, A. Narayanaswamy, X. Chen, and G. Chen, *Appl. Phys. Lett.* **92**, 133106 (2008).
- <sup>19</sup>R. S. Ottens, V. Quetschke, S. Wise, A. A. Alemi, R. Lundock, G. Mueller, D. H. Reitze, D. B. Tanner, and B. F. Whiting, *Phys. Rev. Lett.* **107**, 014301 (2011).
- <sup>20</sup>T. Kralik, P. Hanzelka, M. Zobac, V. Musilova, T. Fort, and M. Horak, *Phys. Rev. Lett.* **109**, 224302 (2012).
- <sup>21</sup>R. St-Gelais, B. Guha, L. Zhu, S. Fan, and M. Lipson, *Nano Lett.* **14**, 6971 (2014).
- <sup>22</sup>T. Ijiri and N. Yamada, *Appl. Phys. Lett.* **106**, 023103 (2015).
- <sup>23</sup>M. Lim, S. S. Lee, and B. J. Lee, *Phys. Rev. B* **91**, 195136 (2015).
- <sup>24</sup>K. Ito, A. Miura, H. Iizuka, and H. Toshiyoshi, *Appl. Phys. Lett.* **106**, 083504 (2015).
- <sup>25</sup>R. St-Gelais, L. Zhu, S. Fan, and M. Lipson, *Nat. Nanotechnol.* **11**, 515 (2016).
- <sup>26</sup>B. Song, D. Thompson, A. Fiorino, Y. Ganjeh, P. Reddy, and E. Meyhofer, *Nat. Nanotechnol.* **11**, 509 (2016).
- <sup>27</sup>S. Basu, B. J. Lee, and Z. M. Zhang, *J. Heat Transfer* **132**, 023301 (2010).
- <sup>28</sup>S. Basu, B. J. Lee, and Z. M. Zhang, *J. Heat Transfer* **132**, 023302 (2010).

# Supplementary Material for Near-Field Radiative Heat Transfer between Doped-Si Parallel Plates Separated by a Spacing down to 200 nm

Jesse I. Watjen,<sup>†</sup> Bo Zhao,<sup>†</sup> and Zhuomin Zhang\*  
George W. Woodruff School of Mechanical Engineering  
Georgia Institute of Technology, Atlanta, GA 30332, USA

## S1. Sample fabrication

To create a nanoscale gap spacing, it is critical to maintain the surface of the sample as flat as possible. Thus, we purchased a set of low-bow 10-cm-diameter Si wafers, about 500  $\mu\text{m}$  thickness, with stringent specifications on the parallelism and flatness. We then measured the surface profile of each wafer using a Bowoptic 208 stress measurement system. Unfortunately, due to stresses within the Si wafer, a typical wafer can have a parabolic deflection profile with about 10-20  $\mu\text{m}$  height variation between the center and the edge. If a 1 cm piece is cut from such a wafer, the Si slab can have a deflection up to 150 nm, which is not readily suitable for use to create a parallel nanoscale gap. This can be seen in Fig. S1(a), which shows the measured surface profile of an as-purchased wafer. The top surface is convex at all the three scan angles: 0°, 45°, and 90°, indicating that deflections of up to 200 nm over 1 cm length of the sample surface are possible and have to be reduced before the wafer is used. Note the cusp that appears at the location of 40 mm is caused by the stitching of multiple sections of the profilometry scan.

Since bow arises from stresses within the wafer, it can be controlled to certain degree by applying a tensile stress via depositing a silicon dioxide layer on one side of the wafer, though the oxide layer generally cannot fix an irregular surface profile such as a saddle shape. Chemical vapor deposition can be used to deposit a stress-free  $\text{SiO}_2$  film at 300°C on the heated Si wafer. After the wafer cools to room temperature, the mismatch in the coefficients of thermal expansion between Si and  $\text{SiO}_2$  causes the wafer to deflect, making the uncoated side less convex. There exists a close-to-linear relationship between the thickness of the oxide and the change in the deflection, but the coefficient in the relationship is different for different wafers. As such, each wafer was tested with an arbitrary film thickness to estimate the correct value of oxide film thickness. After the test, the oxide film was removed using either reactive ion etching or wet etching in a bath of hydrofluoric acid. The profile of the bare surface was remeasured to assure no additional stresses were introduced by the coating and removal process. Subsequently, the correct oxide layer was deposited. Fig. S1(b) shows the effect of the oxide layer on the bow reduction of the top side of the wafer. A 785-nm-thick layer of oxide deposited on the bottom of the wafer changes the radius of curvature of the top surface from about  $-75\text{ m}$  to  $507\text{ m}$  along the 0° scan line. With this procedure, the maximum deflection over the entire top wafer surface can be limited to about 3  $\mu\text{m}$  and the wafer can be used to make samples.

<sup>†</sup> Equal contribution

\* Corresponding author: zhuomin.zhang@me.gatech.edu

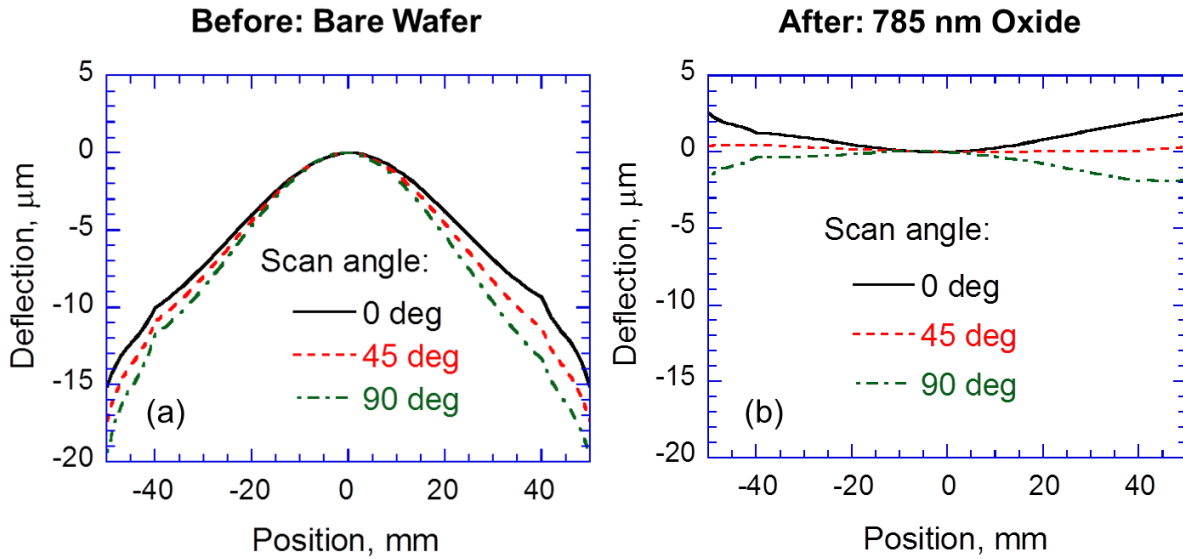


Fig. S1. Surface profile of the top surface of a wafer at different scan angles: a) as-purchased and b) after deposition of a 785 nm silicon dioxide film on the bottom surface. The profiles of the bottom surfaces were not shown.

Before the fabrication, the Si wafer was cleaned using a heated piranha bath to remove organic contaminants. The wafer was then transferred to a PECVD machine (Oxford Instruments Plasmalab 80 Plus) to deposit oxide at a reproducible rate of 62 nm/min. The films deposited are uniform within 10 nm over the inner 4 cm radius of the wafer, which is the area used to fabricate the post arrays. The oxide layer thickness was measured with a Nanospec 3000 reflectometer. As an added precaution for the adhesion of the photoresist, a thin layer of hexamethyldisilazane, Microposit P20 Primer, was applied to the film first and then the photoresist was deposited. Futurrex NR71-3000P negative photoresist was chosen because of the low sidewall profile after development. Both the primer and photoresist were applied using a Karl Suss RC8 spinner. A dark-field right-reading mask was made for the ultraviolet exposure. The mask contains 2D arrays of 1 μm diameter holes with a separation  $S$  being 200 μm, 300 μm, 400 μm, and 500 μm. The development of the photoresist was done in a bath of RD6 developer for approximately 30 s. Then reactive ion etching was used to transfer the pattern from the photoresist to the SiO<sub>2</sub> layer. A Vision 320 reactive ion etching machine was used to remove the SiO<sub>2</sub> not protected by the photoresist. CHF<sub>3</sub> and O<sub>2</sub> gases were introduced to the chamber under a pressure of 5.3 Pa to give an etching rate of approximately 26 nm/min. While this process selectively and anisotropically etches the SiO<sub>2</sub> instead of the Si or photoresist, the etching time was controlled to minimize over-etching that can potentially affect the surface roughness. Then, the photoresist was removed by solvent cleaning with acetone, methanol, and isopropanol, followed by a heated piranha bath. A fresh layer of photoresist was deposited to protect the wafer during the dicing process, in which the patterned wafer was diced to 1 cm<sup>2</sup> square pieces, along with a clean wafer. The patterned and unpatterned pieces were then solvent-cleaned and mated inside a fume hood under a cleanroom environment. It was found that the pieces with a good mating could hold together with some degree of van der Waals forces.

Several patterned pieces not used to make samples were characterized to ensure that the patterns created are as desired. Using a confocal microscope to test the repeatability of pattern transfer, we found that about 98% of the pattern can be successfully transferred while less than 2% of the posts are irregularly shaped due to the photoresist posts falling over during the etching process, likely due to poor adhesion. Figure S2 shows the Scanning Electron Microscope (SEM) image taken with a Hitachi S4700 FESEM for a post of 800 nm height. It confirms that the diameter is 1  $\mu\text{m}$  and the sidewalls can also be seen since the image was taken at a 30° angle. It can be seen that the post is not exactly cylindrical and the top surface has some irregularities as well as reduced area. To consider all the above-mentioned defects, the uncertainty of the cross-sectional area for heat conduction is estimated to be 20%. The fabricated posts were also characterized with Atomic Force Microscopy (AFM) that verifies the height of the post to be consistent with the desired value within about 30 nm height variation.

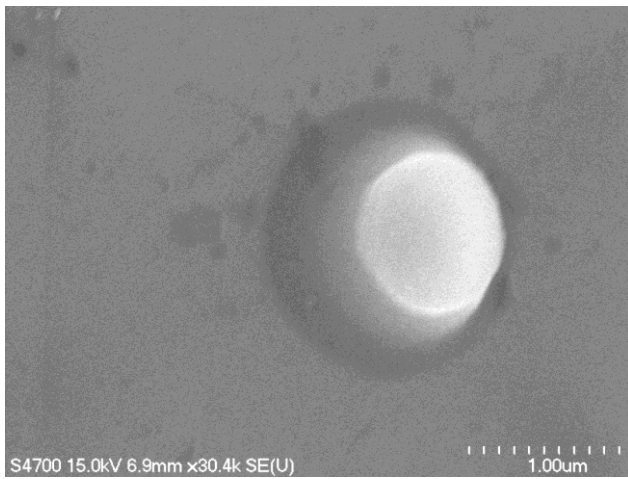


Fig. S2. SEM image of a single post taken at a 30° angle to show the sidewall as well as the top surface.

Through several fabrication attempts, five wafers were successfully patterned to yield a total of 60 samples with  $S = 300 \mu\text{m}$ ,  $400 \mu\text{m}$ , or  $500 \mu\text{m}$ . However, after mating, many samples are not suitable for measurement as the sample either broke, presented an unacceptable gap spacing, or had contact between the two Si pieces. A large portion of these failures is believed to be due to small particles of dust adhering to the surface during the mating process causing mechanical instability and a larger gap spacing. In some cases, the applied grease was too much and the excessive grease can flow over the gap region to create a thermal pathway so that the measured thermal resistance is essentially the contact resistances and the heat flow bypasses the vacuum gap completely. Thus, the overall yield is about 10% if only the five wafers are counted. This does not include the failure and numerous attempts in the earlier attempts of producing patterns. Table S1 lists the detailed information of all the samples presented in this work, corresponding to the 14 measurements shown in Fig. 3. They are listed in chronological order during the near-field heat transfer measurement period from July 2015 to January 2016. For the first three samples measured earlier, no force was applied. The rest samples use different applied forces and are distinguished by letter a, b, c, etc. The post height is based on the film thickness during the fabrication, while the actual spacing  $d$  is determined by FTIR measurements. For each sample and gap spacing, multiple measurements were made with different heater powers as shown in Fig. 2.

Table S1. Details of all the samples used in this work for the 14 measurements.

Wafer No.	Sample No.	Post height (nm)	$S$ ( $\mu\text{m}$ )	Applied force (mN)	FTIR determined $d$ (nm)	Uncertainty of $d$ (nm)	SiO <sub>2</sub> film thickness (nm) patterned side /unpatterned side
1	1	400	300	0	402	70	0/0
1	2	400	500	0	482	40	0/0
2	3	200	400	0	320	80	0/0
3	4a	200	400	0	328	80	595/785
3	4b	200	400	196	200	80	595/785
4	5a	600	500	0	762	30	0/0
4	5b	600	500	127	632	80	0/0
5	6a	800	500	0	782	40	730/785
5	6b	800	500	39	612	50	730/785
3	7a	200	400	0	512	20	595/785
3	7b	200	400	39	484	30	595/785
3	7c	200	400	78	414	60	595/785
3	7d	200	400	118	350	90	595/785
3	7e	200	400	196	336	80	595/785

## S2. Dielectric function of the doped-Si wafers

As mentioned in the paper, there exists a tradeoff between the need for transparency in the near/mid-infrared in order to determine gap spacing and opacity in the mid/far-infrared in order to achieve significant enhancement in near-field radiative heat transfer. While the radiative heat transfer between Si with high doping levels from  $10^{19}$  to  $10^{20}$   $\text{cm}^{-3}$  may be appealing, it cannot be used due to the low transparency in the infrared. Through design calculations, it appears that a  $10^{18}$   $\text{cm}^{-3}$  doping concentration can provide sufficient transparency in the spectral region from  $2000$ - $10000$   $\text{cm}^{-1}$  while supporting large near-field radiative transfer mainly through the spectral region at wavelengths longer than  $5$   $\mu\text{m}$  (or wavenumbers below  $2000$   $\text{cm}^{-1}$ ). Subsequently, we have purchased 10-cm-diameter wafers having a resistivity ranging from  $0.012$ - $0.027$   $\Omega\text{-cm}$  with antimony as the  $n$ -type dopant. This resistivity range corresponds to a doping concentration from  $3 \times 10^{18}$  to  $7 \times 10^{17}$   $\text{cm}^{-3}$ . A Signatone four-point probe measurement system was used to measure the resistivity of the wafers, and the resistivity was found to be  $0.016$   $\Omega\text{-cm}$  averaged over four of the wafers. This gives a doping concentration of  $2 \times 10^{18}$   $\text{cm}^{-3}$ . Before the samples were fabricated, we measured the transmittance ( $T$ ) of all the 25 wafers using an ABB FTLA-2000 FTIR spectrometer and, for some samples, measurements were made at

several different locations. The measurement indeed shows an infrared transparent window. The excellent repeatability and agreement in the measured transmittance suggest that all wafers have the same optical and electronic characteristics. The average thickness of the wafers is  $490\ \mu\text{m}$  with a variation within about  $\pm 10\ \mu\text{m}$  as measured with a micrometer. The spectral reflectance ( $R$ ) of several wafers was measured using a  $10^\circ$  reflectance accessory. The difference is negligibly small when the wafer is flipped, indicating good uniformity and symmetry of these wafers. Nitrogen gas was used to purge the chamber to remove carbon dioxide and water vapor absorption in the measurement. Each measurement is an average of 64 scans with a resolution of  $8\ \text{cm}^{-1}$ . Figure S3 displays the measured average transmittance and reflectance spectra between  $500\ \text{cm}^{-1}$  and  $10000\ \text{cm}^{-1}$ .

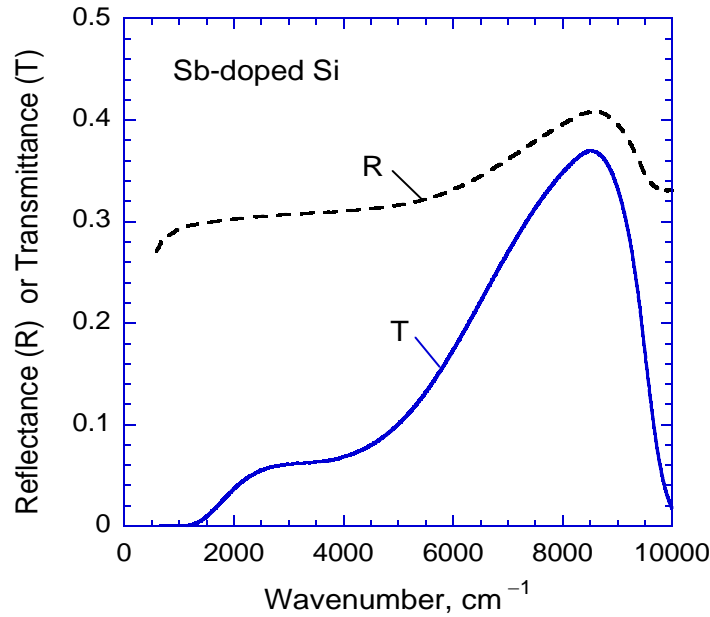


Fig. S3. Spectral reflectance and transmittance of the wafer measured by FTIR.

Initially, a Drude model combined with the bandgap absorption data compiled in Palik<sup>1</sup> were used to model the dielectric function of doped silicon for calculating the reflectance and transmittance. While the agreement is reasonable at wavenumbers below  $2000\ \text{cm}^{-1}$ , discrepancies occur towards large wavenumbers. The shape of the transmittance measurement suggests that there should be some absorption near  $5000\ \text{cm}^{-1}$ , possibly due to unknown impurities or defects in the lattice. A wafer was annealed at  $950^\circ\text{C}$  for two hours at atmospheric pressure but no change in optical properties was measured. As the optical constants in this region are critical for predicting the vacuum gap spacing, we have developed an algorithm to extract the refractive index  $n$  and extinction coefficient  $k$ , at discrete wavenumbers, from the measured  $T$  and  $R$  between  $1500\ \text{cm}^{-1}$  and  $10000\ \text{cm}^{-1}$ .<sup>2</sup> The extracted optical constants are very close to Palik's data at  $9000\text{-}10000\ \text{cm}^{-1}$  due to bandgap absorption and close to that from the Drude model at  $1500\text{-}2000\ \text{cm}^{-1}$ . At lower wavenumbers, the Drude model from Basu et al.<sup>3</sup> was used with a plasma frequency  $\omega_p = 1.47 \times 10^{14}\ \text{rad/s}$ , a scattering rate  $\gamma = 3.53 \times 10^{13}\ \text{rad/s}$ , and a high-frequency constant  $\epsilon_\infty = 11.7$ . The dielectric function of the Drude model can be expressed as

$\varepsilon(\omega) = (n + ik)^2 = \varepsilon_\infty - \omega_p^2 / (\omega^2 + i\omega\gamma)$ . The optical constants combining the Drude model and the extracted values are shown in Fig. S4. The combined optical constants are then used in the calculation of both the reflectance of the sample and the near-field radiative transfer between two Si pieces in the sample. When the back side of the Si wafer is coated with an oxide layer, the reflectance is calculated using the optical constants of SiO<sub>2</sub> from Palik<sup>1</sup> and compared with the FTIR measurements. However, the oxide layer does not affect the near-field radiative heat transfer since the doped-Si wafers are essentially opaque in the mid- to far-infrared region.

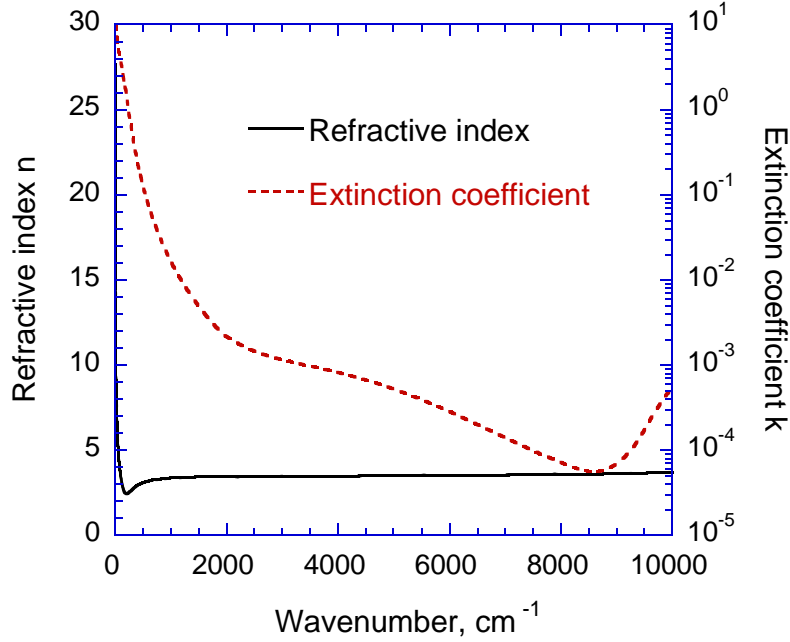


Fig. S4. Optical constants of the Sb-doped Si wafer extracted from the measured radiative properties along with the Drude model for the far-infrared.

### S3. Gap spacing determination

The reflectance spectra of the samples were measured with a PIKE Technologies 10Spec 10° incidence accessory along with the FTIR spectrometer and used for the determination of the gap spacing based on the interference effect of the gap between the Si pieces. A fixture was fabricated and mounted on the top of the reflectance accessory such that a quantifiable force can be applied to the sample, as shown in Fig. S5. A soft spring with a small spring constant is used to apply force on the sample by reducing the height of the supporting bar through its two mounting screws/springs. The springs at the ends support the weight of the supporting bar. The middle spring has a spring constant of 45.5 mN/mm. By measuring the height of the supporting bar or length of the spring with a caliper, the amount of force can be determined based on the spring constant of the middle spring that compresses the sample onto the sample holder. This gives a force resolution of about 12 mN with an uncertainty of about 6 mN, corresponding to a distance interval of 0.13 mm. When fully compressed, a maximum force of 200 mN can be reached. There is an aperture of 3 mm in the middle of the sample holder, which allows the gap

spacing of the sample at different locations to be measured. Gap spacings at different positions across the sample were measured. In some cases, the gap spacing was measured at 9 points on the sample with zero force. There were 5 measurements from one corner of the sample to the opposite corner and then 5 more measurements along the other diagonal, with the center measurement repeated. The change in gap spacing was not significant as compared to the gap spacing uncertainties caused by other mentioned reasons, and should be further mitigated by applying a force. Therefore, the uncertainty caused by the non-parallelism in the samples is neglected. It should be noted that samples with large non-parallelism or with contact at the edges would rule the interference patterns and these samples are excluded from further measurements.

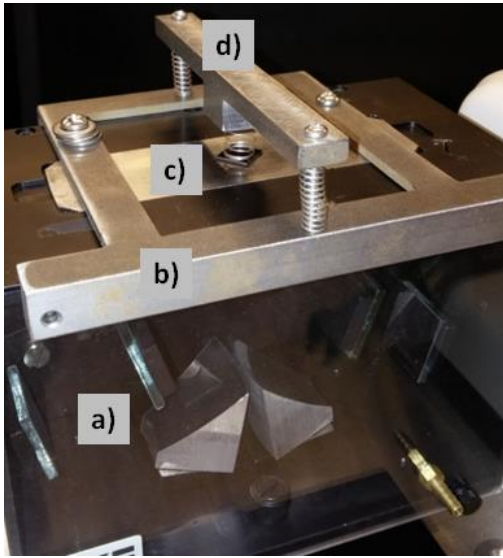


Fig. S5. Photo of the modified reflectance accessory, where the components are indicated by letters as follows: a. PIKE 10Spec setup; b. mounting bracket; c. sample holder with a 3-mm aperture, and d. supporting bar. During the measurement, the sample or a reference is placed under the middle spring and covers the aperture of the sample holder. Force is applied in a similar manner during the heat transfer measurements.

The reflectance measurement was performed using a gold mirror as the reference. The reflectance of the sample is determined by

$$R = R_{\text{Au}} \frac{I_{\text{sam}} - I_{\text{SH}}}{I_{\text{BG}} - I_{\text{SH}}} \quad (\text{S1})$$

where  $R_{\text{Au}}$  is the reflectance of gold.  $I_{\text{BG}}$ ,  $I_{\text{sam}}$ , and  $I_{\text{SH}}$  are the background signal measured using the gold mirror, the signal measured using samples, and the signal measured with an open sample holder, respectively. Measurements were typically made with  $16 \text{ cm}^{-1}$  spectral resolution and a large number of scans up to 512. Predicted reflectance spectra are calculated using a multilayer matrix formulation by treating all layers as coherent.  $\text{SiO}_2$  layers are included for samples that have oxide layers. Since the resolution of FTIR used in the measurement was much larger than the free spectral range of the interference inside the Si wafer, spectral averaging was applied to obtain the spectra that can be compared with experiments. In essence, the coherence exists only in the air gap and the oxide layers, while the Si wafer is a relatively thick slab where interference effects are negligible even though multiple reflections occur.<sup>4</sup>

For samples with applied forces using this fixture, position-resolved measurements were conducted first. This measurement allows us to obtain a rough map of the deflection or non-parallelism between the two Si pieces. Some samples can maintain a consistent gap spacing at the center, while the edges can have contact between the Si pieces; this can be detected from the incoherent feature of the reflectance spectrum. We tested one such sample in the heat transfer experimental setup and the measured  $h_{\text{rad}}$  is about 6.5 times of the calculated value. Thus, these samples are discarded without further investigation. Only the samples that can maintain a gap without contact at the edges were measured under different applied forces, in which case the reflectance of the center of the sample was measured. The measurements started with 0 mN spring force when the spring is fully extended. The supporting bar is loaded and spring length was then reduced to the next desired force. The maximum force was limited to 200 mN considering the yield stress of the SiO<sub>2</sub> and Si and the results from the COMSOL simulation.<sup>2</sup> The force was then unloaded from the maximum load to 0 mN, repeating measurements at the same forces, to guarantee plastic deformation did not occur in the sample.

Figure S6 illustrates the agreement between the measured and calculated reflectance spectra. For each sample, in addition to the calculated spectrum for the best-fitted gap spacing, the calculated spectra for the upper and lower bounds of  $d$  are also shown. Six measurements are shown here with  $d$  ranging from 200 nm to 762 nm according to Table 1, while three of them ( $d = 200$  nm, 402 nm, and 762 nm) are the same as those shown in Fig. 4. Note that the sample with  $d = 200$  nm has 595 nm of oxide film on the back of the patterned piece and 785 nm of oxide film deposited on the back of the unpatterned piece. Similarly, the sample with  $d = 612$  nm has a 730 nm oxide film deposited on the back side of the patterned piece and 785 nm of oxide film deposited on the back of the unpatterned piece.

Calculated spectra with different gap spacings are compared with the measured spectrum to find the standard error of the estimate (SEE), which is essentially the same as the root-mean-square deviation for all the measured wavenumber points. In calculating SEE, the spectral range 1500 cm<sup>-1</sup> to 10000 cm<sup>-1</sup> was considered for the samples with oxide, while for the samples without oxide, 4000 cm<sup>-1</sup> to 10000 cm<sup>-1</sup> was considered since the major difference of the reflectance spectra occurs in these ranges. The gap spacing  $d$  is determined when SEE becomes the smallest, as illustrated in Fig. S7 for three measurements. To estimate the uncertainty in the fitted gap spacing, we let the SEE value increase by 0.005, such that the upper and lower value of the gap distance can be found. The uncertainty of the gap spacing is calculated as half of the difference between the upper and lower values. The determined gap spacings and the associated uncertainties are shown in Table S1. The uncertainty value for each sample is used as the upper and lower limits of  $d$  in plotting the reflectance spectra shown in Fig. S6.

In some cases, the SEE reaches a local minimum at more than one gap spacing and the most reasonable one is chosen as the fitted  $d$ . For example, for the  $d = 512$  nm sample, another local minimum is found at  $d = 114$  nm but the SEE value is obviously much higher. The situation for  $d = 200$  nm sample is somewhat different, as can be seen in Fig. S7, the SEE value is lower at the local minimum of  $d = 426$  nm than at  $d = 200$  nm. In this case, since the  $d$  value without spring force is already 328 nm (see Table S1), upon applied force, it is logical to take  $d = 200$  nm as the fitted value. It should be noted that, for certain samples, the reflectance spectra are almost indistinguishable for a relatively large range of  $d$  values. For the sample shown in the diamond

symbol in Fig. 3, the SEE values change little for  $260 \text{ nm} < d < 340 \text{ nm}$ , as shown in Fig. S7. Even though  $d = 336 \text{ nm}$  gives the minimum SEE, reducing  $d$  to  $290 \text{ nm}$  only increases SEE by  $0.001$ . If a value of  $d = 290 \text{ nm}$  was used, the experimentally determined  $h_{\text{rad}}$  would be reduced due to the increased conduction contribution but the numerically calculated  $h_{\text{rad}}$  would increase due to the reduced gap spacing, resulting in a good agreement within the uncertainties.

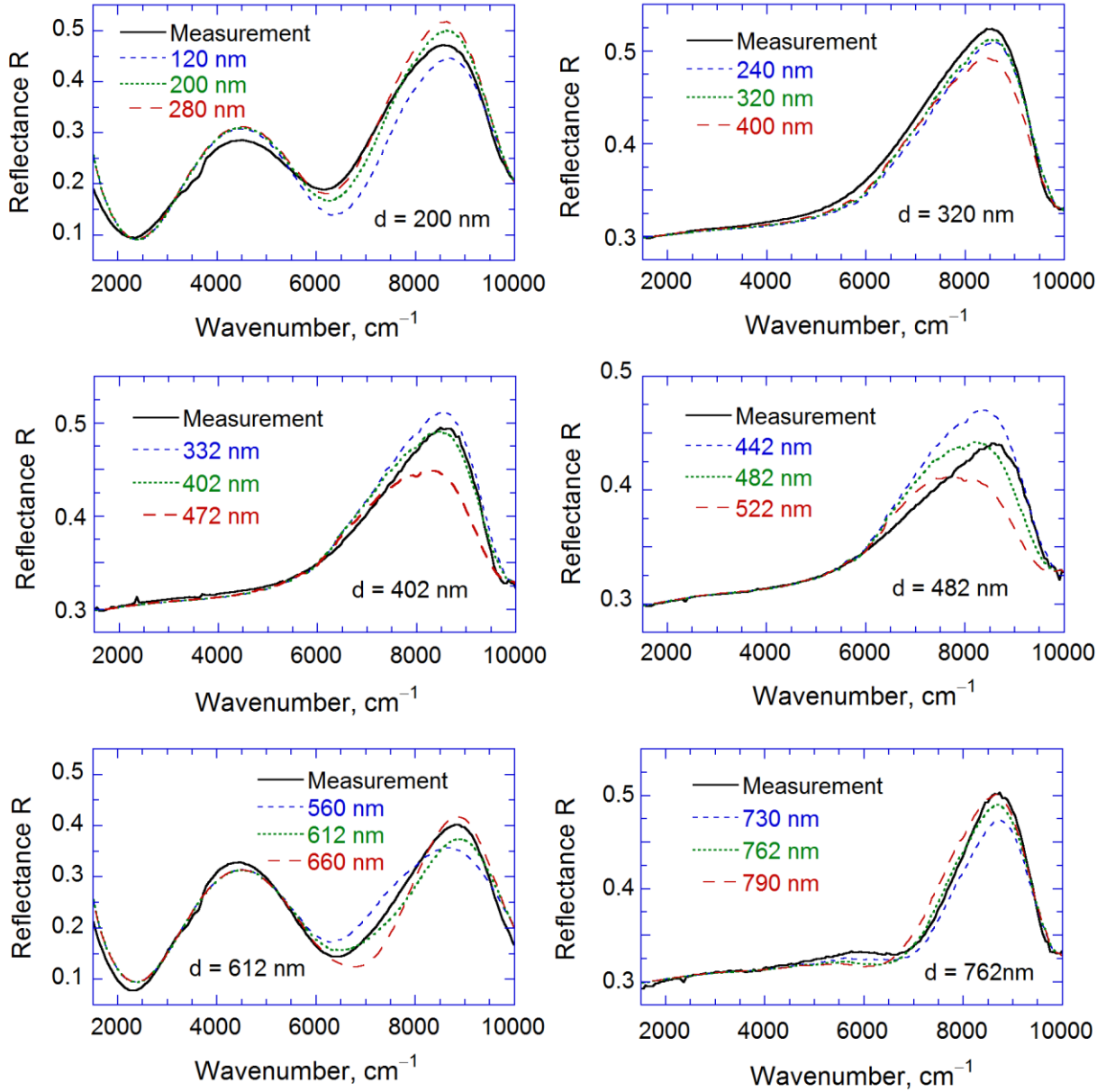


Fig. S6. Determination of the gap spacing using the reflectance spectra. The spectrum of the determined gap spacing is compared with the measurement together with the spectrum after the uncertainty of the gap spacing is considered.

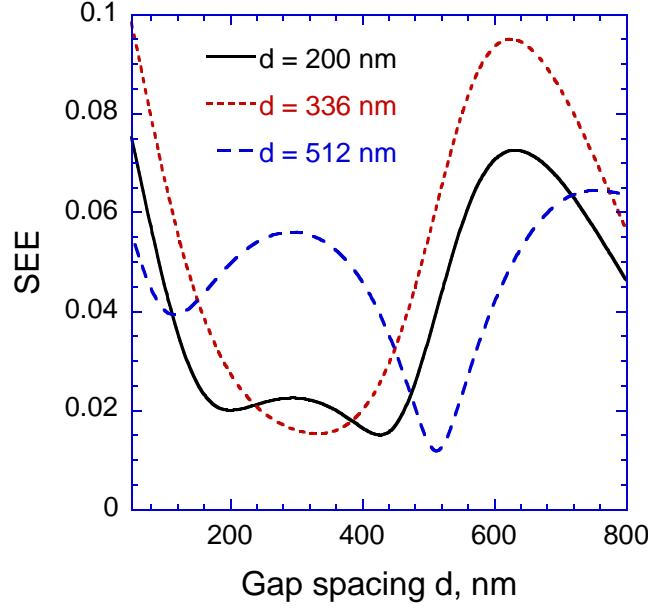


Fig. S7. The standard error of estimate (SEE) between the calculated and measured reflectance as a function of  $d$  in the calculation for three measurements.

#### S4. Calculation of near-field thermal radiation

The origin of the strong near-field heat transfer can be explained by the spectral radiative heat flux,  $q''_{\omega}$ , between two semi-infinite doped-Si media, which is obtained from fluctuational electrodynamics using dyadic Green's functions:<sup>4,5</sup>

$$q''_{\omega} = \frac{1}{4\pi^2} \int_0^{\infty} \xi(\omega, \beta) [\Theta(\omega, T_H) - \Theta(\omega, T_L)] \beta d\beta \quad (\text{S2})$$

Here,  $\Theta(\omega, T) = \hbar\omega / [\exp(\hbar\omega/k_B T) - 1]$  is the average energy of a Planck oscillator, where  $\hbar$  is the reduced Planck constant,  $\omega$  is the angular frequency and  $k_B$  is the Boltzmann constant. In Eq. (S2),  $\beta$  represents the magnitude of the wave vector parallel to the heat transfer interface, and  $\xi(\omega, \beta)$  is the photon tunneling probability (also called energy transmission coefficient) that includes both polarizations. Equation (S2) is integrated to obtain the total radiative heat transfer rate or heat transfer coefficient as shown in Figs. 2 and 3. The predicted spectral heat flux is shown in Fig. S8 with various gap spacings, when the emitter and receiver temperatures are set to 320 K and 300 K, respectively. Two peaks can be identified on the plot especially at small gap spacings. The sharp peak at the lower frequency is caused by the high density of states of coupled surface plasmon polaritons (for transverse magnetic waves only) when the real part of the dielectric function of doped-Si is around  $-1$ , and the other broader peak is due to the frequency dependence of the Planck oscillator.<sup>4</sup> Since the field intensity of surface plasmons exponentially decay away from the interface, a smaller gap distance promotes the coupling of surface plasmons at the vacuum-Si interfaces, mediating more efficient photon tunneling at large  $\beta$  and resulting in higher spectral heat flux.<sup>5</sup>

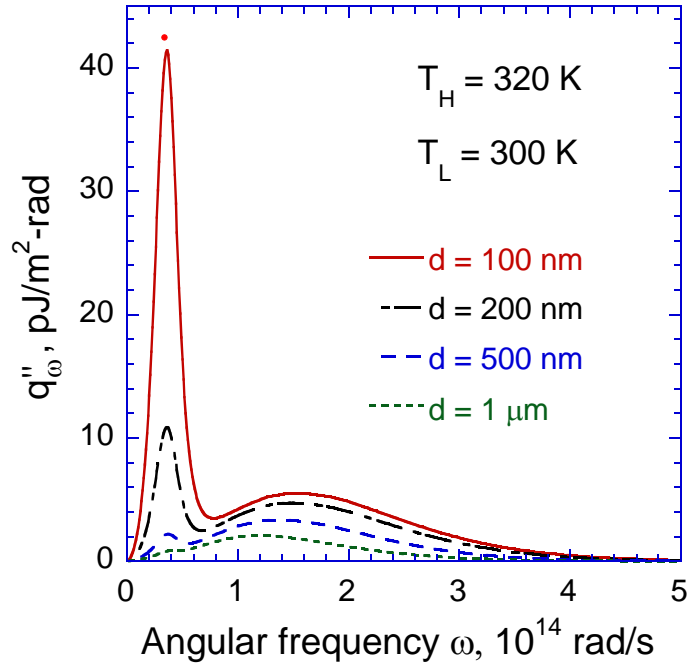


Fig. S8. Calculated spectral radiative heat flux at different gap spacings based on fluctuational electrodynamics. The emitter and receiver temperatures are 320 and 300 K, respectively.

## S5. Uncertainty analysis

The uncertainty in  $d$  is relatively large and it affects the calculated results and the determination of the contribution of heat conduction. In the measurements, the samples were mounted on the stack and a spring (same as the one in the force-controlled FTIR reflectance measurements) was used on top of the heater. The length of the spring was measured and the amount of force applied to the sample can be calculated. The uncertainty of  $d$  is determined for each sample based on the FTIR measurements displayed in Table S1. Additionally, since the applied force has uncertainty (about 6 mN) and the weight of the components above the sample (about 20 mN) can also bring uncertainty to the applied force, an uncertainty of 20 nm in gap spacing is considered to be combined with the uncertainty determined from the FTIR measurements.

The LakeShore DT-670 silicon diode thermistor is calibrated by the manufacturer and tested to be accurate within 37 mK in the temperature range used here. The uncertainty of the temperature comes from the thermoelectric circuit. It is made of two Omega 40AWG E-type thermocouples by bonding the constantan wires together using a thermocouple welder, such that the output voltage can be directly used to obtain the temperature difference between the two normal chromel-constantan junctions. The uncertainty of the thermoelectric circuit is 0.15°C determined by calibration using an Engineering Model 12001-A-12-6-2-A/LT14 resistance thermal detector.<sup>2</sup>

The measured radiative heat transfer rate is obtained by excluding the conduction contribution from the measured heat rate, i.e.,  $q_{\text{rad}} = q_{\text{HFM}} - q_{\text{cond}}$ . Thus, the uncertainty of the measured  $q_{\text{rad}}$  depends on the total heat rate measurement and the conduction estimation. The uncertainty of  $q_{\text{rad}}$  as well as  $h_{\text{rad}}$  can be determined based on an error propagation analysis. The uncertainty of the heat flux meter is estimated to be 4.4% as determined from a calibration experiment using PTFE samples whose thermal conductivity were determined by measuring the specific heat and the thermal diffusivity using a differential scanning calorimeter and a light flash technique, correspondingly.<sup>2</sup> The resulting value for the sensitivity is  $6.87 \mu\text{V}\cdot\text{cm}^2/\text{mW}$ , as compared with  $7.88 \mu\text{V}\cdot\text{cm}^2/\text{mW}$  provided by the manufacturer since the manufacturer's calibration was not done with the same setup.

The heat conduction rate is calculated using a simple one-dimensional conduction model by assuming all the posts have the same height  $d$ . Since the thermal resistance associated with crossing the vacuum gap is so much larger than the lateral resistance in the silicon plates, the temperature is assumed to be uniform with each Si piece. Hence, the heat transfer rate by conduction is found as

$$q_{\text{cond}} = N_{\text{post}} \frac{\kappa A_{\text{post}}}{d} \Delta T \quad (\text{S3})$$

where  $A_{\text{post}}$  is cross-sectional area of each post and the number of posts is  $N_{\text{post}} = 1 \text{ cm}^2 / S^2$ . The value of thermal conductivity of  $\text{SiO}_2$  is taken as  $1.4 \pm 0.1 \text{ W/m}\cdot\text{K}$ , considering the possible effects of phonon-boundary scattering. The number of posts is assumed to have no uncertainties, while in contrast the uncertainty is considered as 20% in the cross-sectional area of the post.

It should be noted that using such a model to calculate the conduction is not ideal; however, fully quantifying the conduction is very challenging using current techniques. This would require complete knowledge of the height distribution and contact area of the posts, the thermal contact resistance between the  $\text{SiO}_2$  posts and the Si wafer, the exact surface profiles of both pieces, and the way that the sample deforms when external forces are applied, etc. Many of these factors are expected to vary between samples and *in situ* measurements would be required for unambiguous determinations. Considering this, the above-mentioned model was used to calculate the conduction contribution with a rather large estimated uncertainty to compensate for the difficulties in accurate determination of heat conduction. This can be a major limitation of current experiment design and may be improved in future works.

It is important to limit the conduction heat transfer in many practical applications utilizing near-field thermal radiation. Reducing the conduction heat transfer can also improve the near-field radiation measurement accuracy. Figure S9 shows the contribution of radiation to the total heat transfer. It can be seen that the radiation contribution is above 65%, except for Sample 1 ( $S = 300 \mu\text{m}$  and  $d = 402 \text{ nm}$ ) for which conduction contributes 44% to the heat transfer.

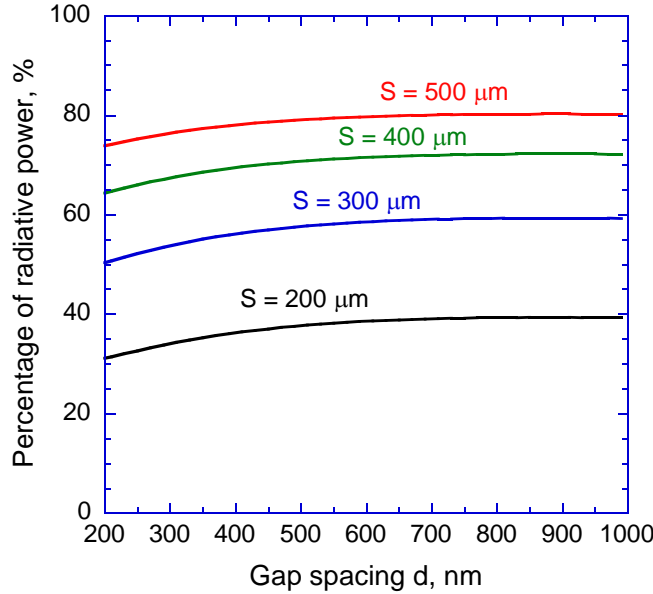


Fig. S9. Percentage of radiative power versus gap spacing for different  $S$  values.

The theoretical calculated  $q_{\text{rad}}$  and  $h_{\text{rad}}$  are subject to uncertainties due to the gap spacing determination and the temperature measurements. The uncertainties in the temperatures of the emitter and receiver only slightly affect the calculated values. If the plasma frequency and the scattering rate used in the Drude model are individually varied or both varied in the same or opposite directions within 10%, the resulting radiative heat transfer rate deviates within 5%. The uncertainties in the optical constants and sample areas are thus neglected in the determination of the error bounds shown in Figs. 2 and 3. The uncertainty in the calculated  $q_{\text{rad}}$  or  $h_{\text{rad}}$  is dominated by the large uncertainty in the gap spacing determination.

## References

- <sup>1</sup> E. D. Palik, *Handbook of Optical Constants of Solids* (Academic Press, San Diego, CA, 1985).
- <sup>2</sup> J. I. Watjen, Ph.D. Dissertation, Georgia Institute of Technology, May, 2016.
- <sup>3</sup> S. Basu, B. J. Lee, and Z. M. Zhang, *J. Heat Transfer* **132**, 023301 (2010).
- <sup>4</sup> Z. M. Zhang, *Nano/Microscale Heat Transfer* (McGraw-Hill, New York, 2007).
- <sup>5</sup> X. L. Liu, L. P. Wang, and Z. M. Zhang, *Nanoscale Microscale Thermophys. Eng.* **19**, 98 (2015).